

Spectral encoding method for measuring the relative arrival time between x-ray/optical pulses

M. R. Bionta, N. Hartmann, M. Weaver, D. French, D. J. Nicholson, J. P. Cryan, J. M. Glowina, K. Baker, C. Bostedt, M. Chollet, Y. Ding, D. M. Fritz, A. R. Fry, D. J. Kane, J. Krzywinski, H. T. Lemke, M. Messerschmidt, S. Schorb, D. Zhu, W. E. White, and R. N. Coffee

Citation: [Review of Scientific Instruments](#) **85**, 083116 (2014); doi: 10.1063/1.4893657

View online: <http://dx.doi.org/10.1063/1.4893657>

View Table of Contents: <http://scitation.aip.org/content/aip/journal/rsi/85/8?ver=pdfcov>

Published by the [AIP Publishing](#)

Articles you may be interested in

[X-ray–optical cross-correlator for gas-phase experiments at the Linac Coherent Light Source free-electron laser](#)
Appl. Phys. Lett. **100**, 121107 (2012); 10.1063/1.3695163

[Linac Coherent Light Source soft x-ray materials science instrument optical design and monochromator commissioning](#)
Rev. Sci. Instrum. **82**, 093104 (2011); 10.1063/1.3633947

[Femtosecond synchronism of x-rays and visible/infrared light in an x-ray free-electron laser](#)
Rev. Sci. Instrum. **78**, 123302 (2007); 10.1063/1.2805114

[Erratum: “Thermal stresses in the reflective x-ray optics for the Linac Coherent Light Source” \[Rev. Sci. Instrum. 74, 3722 \(2003\)\]](#)
Rev. Sci. Instrum. **75**, 5059 (2004); 10.1063/1.1804975

[Xray Optics Research for Linac Coherent Light Source: Interaction of Ultrashort Xray Pulses with Matter](#)
AIP Conf. Proc. **641**, 596 (2002); 10.1063/1.1521083

The advertisement for Saes Group features a red square logo with the text 'saes group' in white. To the right of the logo is a photograph of four x-ray optics components, which are cylindrical metal structures mounted on red square bases. Below the logo, the email address 'neg_technology@saes-group.com' and the website 'www.saesgroup.com' are listed in red text.

Spectral encoding method for measuring the relative arrival time between x-ray/optical pulses

M. R. Bionta,^{1,2,3,a)} N. Hartmann,^{3,4} M. Weaver,³ D. French,^{3,b)} D. J. Nicholson,^{3,5} J. P. Cryan,^{6,b)} J. M. Glowina,³ K. Baker,⁷ C. Bostedt,³ M. Chollet,³ Y. Ding,³ D. M. Fritz,³ A. R. Fry,³ D. J. Kane,⁸ J. Krzywinski,³ H. T. Lemke,³ M. Messerschmidt,^{3,b)} S. Schorb,^{3,b)} D. Zhu,³ W. E. White,³ and R. N. Coffee^{3,9,c)}

¹Université de Toulouse, UPS, Laboratoire Collisions Agrégats Réactivité, IRSAMC, F-31062 Toulouse, France

²CNRS, UMR 5589, F-31062 Toulouse, France

³The Linac Coherent Light Source, SLAC National Accelerator Laboratory, 2575 Sand Hill Road, Menlo Park, California 94025, USA

⁴Institute of Applied Physics, University of Bern, Sidlerstr. 5, 3012 Bern, Switzerland

⁵Department of Applied Physics, Stanford University, Stanford, California 94305, USA

⁶Lawrence Berkeley National Laboratory, 1 Cyclotron Road, Berkeley, California 94720, USA

⁷Lawrence Livermore National Laboratory, P.O. Box 808, Livermore, California 94551, USA

⁸Mesa Photonics, LLC., 1550 Pacheco St., Santa Fe, New Mexico 87505, USA

⁹The PULSE Institute for Ultrafast Energy Science, SLAC National Accelerator Laboratory, 2575 Sand Hill Road, Menlo Park, California 94025, USA

(Received 18 March 2014; accepted 10 August 2014; published online 28 August 2014)

The advent of few femtosecond x-ray light sources brings promise of x-ray/optical pump-probe experiments that can measure chemical and structural changes in the 10–100 fs time regime. Widely distributed timing systems used at x-ray Free-Electron Laser facilities are typically limited to above 50 fs fwhm jitter in active x-ray/optical synchronization. The approach of single-shot timing measurements is used to sort results in the event processing stage. This has seen wide use to accommodate the insufficient precision of active stabilization schemes. In this article, we review the current technique for “measure-and-sort” at the Linac Coherent Light Source at the SLAC National Accelerator Laboratory. The relative arrival time between an x-ray pulse and an optical pulse is measured near the experimental interaction region as a spectrally encoded cross-correlation signal. The cross-correlation provides a time-stamp for filter-and-sort algorithms used for real-time sorting. Sub-10 fs rms resolution is common in this technique, placing timing precision at the same scale as the duration of the shortest achievable x-ray pulses. © 2014 AIP Publishing LLC. [<http://dx.doi.org/10.1063/1.4893657>]

I. INTRODUCTION

One of the motivations for the development of x-ray Free Electron Lasers (xFELs) rests on their use in determining the few femtosecond chemical dynamics that lead to the exquisite efficiencies found in natural chemical reactions. Towards this end, few femtosecond x-ray pulses are routinely used at the Linac Coherent Light Source (LCLS) xFEL at the SLAC National Accelerator Laboratory (SLAC) in Menlo Park, CA.¹ X-ray pulses with sub-10 fs durations are becoming common at other xFEL facilities.^{2–11}

At these facilities, achieving fine time resolution with active control of x-ray/optical delay is extremely cumbersome if not impossible. Although precise optical synchronization can exist in direct laser seeding schemes,⁸ such techniques may not extend to harder x-ray sources where direct laser seeding is more difficult. Currently, active stabilization of independent laser oscillators can provide better than 10 fs root mean square (rms) jitter⁸ for in-loop phase noise measurement, and better ~25 fs rms jitter for arrival time feedback based systems;¹²

propagation of errors through beam transport may degrade this best-case scenario. More typically, phase-locking of conventional accelerators and laser systems such as at the LCLS typically only hold the jitter to about 250 fs full width at half maximum (fwhm).¹³ We therefore seek a solution more reminiscent of the style of event-based data processing that evolved within the field of high energy particle physics. In high energy collisions, the community developed data acquisition and analysis frameworks based on recording as many of the parameters as possible for analysis in post-processing. At the LCLS, many parameters associated with the x-ray pulse cannot be controlled and so must be recorded on every event and used in a measure-and-sort strategy.^{14–17} In the case of spectral-encoding reviewed here, the measurement tags experimental events with a relative arrival time that is then used to time-order the results with ~10 fs rms level resolution.^{18,19}

The spectral-encoding method uses a broadband supercontinuum as an optical probe pulse.²⁰ The supercontinuum pulse is chirped (non-zero group delay dispersion (GDD)) such that different frequency components arrive at slightly different times, thus providing a low-order polynomial mapping of wavelength to time. In order to imprint the x-ray arrival on the probe spectrum, we pass the supercontinuum probe simultaneously with the x-ray pulse through optically transparent samples, typically silicon nitride (Si₃N₄)

^{a)}Electronic mail: mina.bionta@irsamc.ups-tlse.fr

^{b)}This research was performed while D. French, J. P. Cryan, M. Messerschmidt, and S. Schorb were at The Linac Coherent Light Source, SLAC National Accelerator Laboratory, 2575 Sand Hill Road, Menlo Park, California 94025, USA.

^{c)}Electronic mail: coffee@slac.stanford.edu

membranes, quartz (SiO_2) crystals, or cerium doped yttrium aluminum garnet (Ce:YAG , $\text{Ce:Y}_3\text{Al}_5\text{O}_{12}$). The x-ray induced change in the complex index of refraction of the material modulates the amplitude and phase of the super-continuum. This modulation produces a feature in the transmitted spectrum, the location of which represents the arrival time of the x-rays via the low-order polynomial mapping.^{21,22} The frequency to time mapping allows for a tunable temporal window due to the adjustability of the continuum chirp (GDD). In addition to the tunable window, the method does not need an extended spatial sample range and therefore can be measured with a focused continuum probe. This makes it insensitive to spatial mode imperfections in the x-ray beam profile. Such flexibility and robustness are major attractions of the method.

In this review, we describe the spectral-encoding measurement that has become a standard relative timing diagnostic at the LCLS. We will review the following:

- relative delay encoding with the desired sub-10 fs rms resolution²³ in both the hard and soft x-ray regimes,^{18,19,24}
- typical geometry as implemented at the LCLS,
- principle of the acquisition routine and the analysis software that extracts the arrival time,
- an alternative algorithm for off-line time-sorting in post-analysis,
- geometric considerations that determine the efficacy of this technique.

II. EXPERIMENTAL DETAILS

The typical experimental geometry is shown in Fig. 1. A broadband continuum is generated by focusing $\sim 1 \mu\text{J}$ of a ~ 40 fs Ti:Sapphire laser pulse into a 1 mm thick C-cut sapphire plate. Self-phase modulation in the sapphire produces a 400 nm broad super-continuum of which a smooth spectral intensity and phase portion from 450 to 680 nm (2.8–1.8 eV) is used for the spectrum to time mapping. The continuum probe is chirped to ~ 1.5 ps by accumulating GDD in an achromatic re-collimating lens, an optional Wollaston prism polarizer, final focusing lens, and a vacuum in-coupling window. The Wollaston prism polarizer allows us to send a cross-polarized replica with two foci—one beam forms a spatially displaced focus that misses the x-ray pumped region but otherwise co-propagates with the probe pulse through the entire optical setup. Such a reference can be used as a single shot reference, removing any fluctuations in the probe spectrum. Since the two cross-polarized pulses are not identical in spectral intensity, or more often referencing is not used, we can use a fast switching dipole magnet to deflect the electron bunch before the FEL undulators. This suppresses x-ray lasing for every n th shot of the accelerator, allowing for a rolling accumulation of reference and un-pumped probe spectra. Choosing n to be a prime number, usually 5, 11, or 19, we reduce the effect of systematic correlations of FEL parameters with electrical power line phase. These un-pumped shots provide the transfer function for the spurious differences in the single-shot referencing scheme. We note that extra care

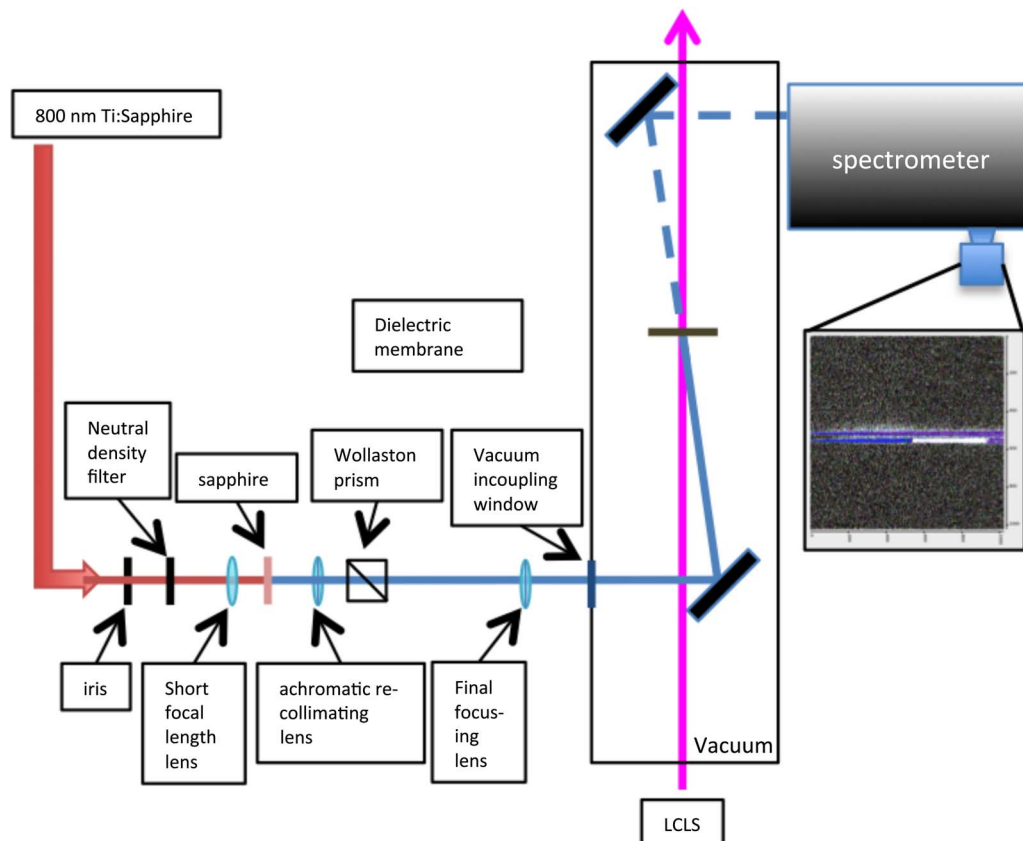


FIG. 1. Experimental geometry. As discussed in the text, a broadband super-continuum intersects the x-ray beam in a semiconductor membrane and is then spectrally dispersed onto a fast readout CCD array.

TABLE I. Summary of sampled materials with corresponding refractive indices (real part, n_{vis}), band gaps, and x-ray absorption lengths for various photon energies^{28–30} and sample thicknesses and their resulting nominal geometric smearing used at the LCLS.

Sample	n_{vis} at 550 nm	Band gap	X-ray energies	Absorption length	Sample thickness	Nominal geometric smearing
Amorphous Si ₃ N ₄	2.0	5 eV	1 keV	21 μ m	500 nm	0.3 fs
			4.5 keV	14 μ m	500 nm	0.3 fs
			7 keV	51 μ m	2 μ m	1.3 fs
			9 keV	107 μ m	2 μ m	1.3 fs
Single crystal quartz	1.55	9 eV	4.5 keV	20 μ m	150 μ m	77 fs
					75 μ m	39 fs
			9 keV	144 μ m	150 μ m	77 fs
					75 μ m	39 fs
Chemical Vapor Deposition (CVD) diamond	2.4	5.5 eV	1 keV	23.3 μ m	500 μ m	400 fs
			4.5 keV	5110 μ m	55 μ m	44 fs
			9 keV	947.9 μ m	55 μ m	44 fs
Crystalline Ce:YAG	1.84	7.01 eV	4.5 keV	6.2 μ m	50 μ m	31 fs
Ce:Y ₃ Al ₅ O ₁₂			9 keV	41.6 μ m	50 μ m	31 fs
Crystalline gadolinium	2 ³¹	4 eV	4.5 keV	4.2 μ m	500 μ m	333 fs
Gallium garnet (Gd ₃ Ga ₅ O ₁₂)			9.5 keV	9.1 μ m	500 μ m	333 fs
Single crystal Si	4.09 ³²	1.19 eV	550 eV	0.5 μ m	2 μ m	2.7 fs
			1 keV	35.7 μ m	2 μ m	2.7 fs
			1.8 keV	12.7 μ m	2 μ m	2.7 fs
			1.9 keV	1.4 μ m	2 μ m	2.7 fs
			4.5 keV	12.7 μ m	1 μ m	1.4 fs
			7 keV	43.9 μ m	5 μ m	6.8 fs

should be taken to minimize the effects from mechanical vibrations as well as air currents.

The frequency to time mapping allows for a tunable temporal window since the chirp can be increased by inserting additional material or can be reduced with a prism-pair, grating, or chirped-mirror compressor. Full compression is not desired since residual positive dispersion in the continuum gives the low-order polynomial mapping of frequency to time. We typically use highly dispersive achromatic lenses for the collimation and refocusing of the super-continuum into the sample material. From this, a temporal window of about 1–3 ps for the combination of about 200 nm of bandwidth, generated in 1 mm thickness of sapphire, collimated and focused with standard $f = 50$ –100 mm visible achromatic lenses through a vacuum in-coupling window. At its 1 ps minimum, this window spans three times the temporal jitter experienced at LCLS. Furthermore, users typically make delay scans on the 1–2 ps scale and so we do not usually implement a dispersive compression scheme to decrease the temporal window. We have at times inserted up to 25 mm of BK7 glass to expand the temporal window to over 6 ps.

For the samples used, the refractive index for the x-rays is slightly less than 1, making the biggest contributor to temporal smearing the group delay mismatch (e.g., 250 fs for 150 μ m quartz). The continuum passes through the interaction region at a slight crossing angle as seen in Fig. 1. The crossing angle is at most 100 mrad which corresponds to a geometric smearing of $\frac{nT}{c} \sin \theta$ where T is the thickness of the interaction length, n is the refractive index in the visible, and c is the speed of light. To estimate the scale of this smearing, we assume an even interaction through the 2 μ m thick-

ness of the material. Assuming a refractive index of $n = 2$ (corresponding to that of Si₃N₄ at 550 nm) and the maximum 100 mrad crossing angle yields a ~ 1.3 fs for the geometric effect of temporal smearing in Si₃N₄. This is small enough that the induced time smear does not compromise the timing measurement but large enough that none of the continuum is clipped by mirrors. On the other hand, if we assume an even deposition into quartz where $T = 150$ μ m and $n = 1.5$, we get a nominal geometric smearing of about 77 fs. By nominal smearing, we are neglecting the x-ray induced time dependent refractive index as the plasma front propagates through medium. The exact dispersive dynamics are the subject of extensive plasma filamentation research beyond the technique review of this article.^{20,25,26} The nominal geometric smearing for the sample materials and thicknesses used at the LCLS are given in Table I.

The continuum is spectrally resolved in a Princeton Instruments Acton SP2500 spectrometer with a 50 lines/mm groove density reflective grating blazed for 600 nm first order diffraction. The 6 mm horizontal dimensions of the 1024 \times 1024 pixel CCD array used as the detector correspond to ~ 200 nm bandwidth acceptance. The CCD is an Opal 1000 detector with 120 Hz readout into the data stream. We image the continuum focus at the interaction region onto the entrance slit of the spectrometer to fill the $f/6$ imaging of the spectrometer. The pixel to wavelength calibration is made by measuring known atomic lines from an Ocean Optics HG-1 mercury/argon low-pressure gas source. The measured spectral resolution is 0.217 nm with an error of 1%.

It has been suggested that using the ~ 30 nm bandwidth of amplified Ti:Sapphire pulses directly, without converting

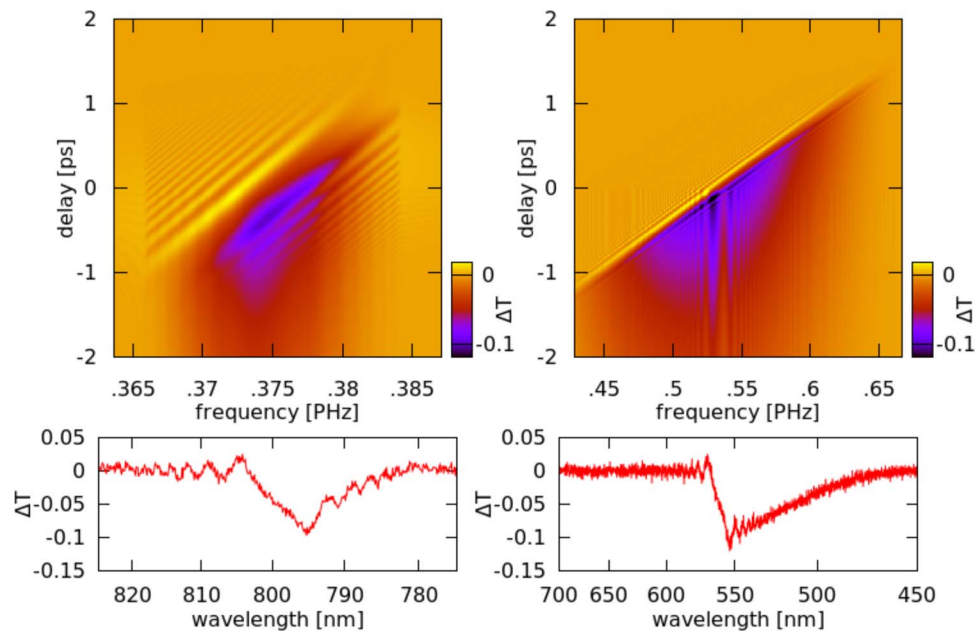


FIG. 2. Resolution versus spectrum. We compare simulations for broad-band visible continuum (right) versus a narrower bandwidth version (left). We find that although the interference is much more pronounced with narrow bandwidth, the noise reduces the required fidelity to make full use of the narrow-band fringes.

to a continuum, would provide a more stable measurement scheme. This, however, is equivalent to increasing the chirp/bandwidth ratio for a given time window. Figure 2 compares simulations for the typical 1.5 ps window covered by either the 200 nm of visible spectrum versus 30 nm of infrared spectrum. From this figure we can see that the edge which indicates the arrival time is much sharper when more bandwidth is available. The higher number and more pronounced oscillations in the narrower 30 nm band version could alleviate the loss of precision due to the narrower bandwidth. Nevertheless, in this review we focus on a sharper edge by using a broad spectrum.

A monotonic spectrum to time mapping is required for this technique. The shot-to-shot stability of the phase coefficients for such a technique is sufficient for precision measurements of time.^{21,23} It is typical in such a measurement to use positive dispersion, when long wavelengths arrive before short, even though excitation induced by the probe is negligible for materials with direct or indirect band gaps on the order of 5–9 eV for these intensities. Since the continuum extends from about 1.8–2.8 eV, we are probing below the band gap. The preference for positive dispersion becomes more important as we explore lower band-gap materials where the blue end of the visible spectrum begins to absorb into the material.

An interesting corollary arises when using experimental laser wavelengths that lie within the continuum band; one can then use the super-continuum to find temporal overlap between the x-ray pulses and the experimental optical laser pulses. Often an experiment may not give a clear signal of temporal overlap in the main experimental chamber since the timing arm and experimental arms follow separate paths to separate interaction chambers. If the experimental laser can be leaked into a downstream timing chamber, time overlap between the super-continuum and the experimental arm can be found with spectral interferometry. Spectral fringes appear

at the wavelength of the experimental pulse where the density of the fringes is linearly proportional to the time separation between the experimental and timing pulses. The main laser can then be brought into time-overlap with the x-ray pulse by putting the spectral feature of the x-rays on the super-continuum to the same region as the experimental laser and by minimizing the fringe density in the main-laser/continuum interference.

A. Experimental procedure

A typical x-ray/optical time-overlap routine consists of the following:

- Measure the x-ray pulses and super-continuum pulses with an externally triggered ≥ 13 GHz bandwidth oscilloscope that reads the output waveform of a ~ 50 GHz x-ray/optical metal-semiconductor-metal (MSM) diode signal. This routinely achieves a coarse timing resolution of 10–30 ps.
- Binary search of the changing etalon effect in spectral transmission. This typically locates time overlap to within 500 fs; within the continuum window itself.
- Measure the spectral chirp by scanning the optical delay, either mechanically with a delay stage or electronically with an arbitrary phase angle in the RF synchronization loop. Plot the correlation of edge position versus delay setting and fit with a second order polynomial. The polynomial then gives a mapping relation for the position and relative delay in femtoseconds for the course of the run.

III. FITTING

The relative arrival time is located by applying a matched digital filter to the spectral change in transmission. Digital

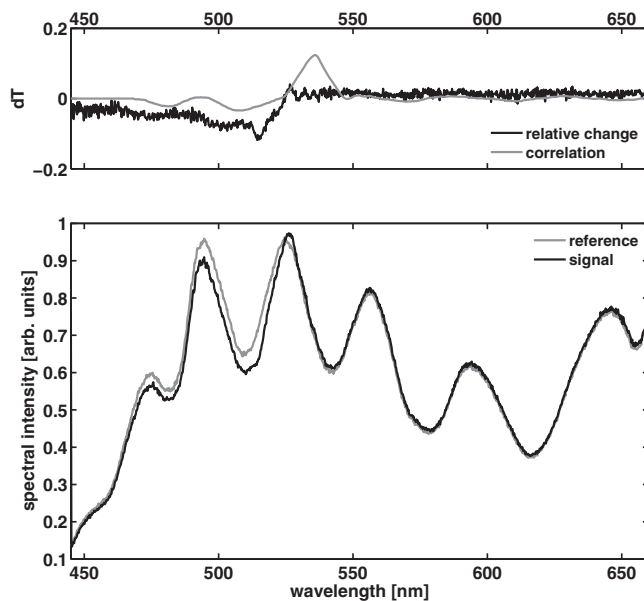


FIG. 3. Fitting. The bottom panel shows an example signal (black) and reference (gray) spectrum. The time encoding is such that shorter wavelengths arrive later in time than longer wavelengths. The change in transmission for $2\ \mu\text{m}$ Si_3N_4 can be seen as the difference between these two traces and is shown in the top panel. The relative change in transmission is shown in black, and the correlation of the optimal waveform and the measured signal, as discussed in the text, is shown in gray.

matched filtering is a common deconvolution technique used in linear signal analysis.²⁷ This method requires a known detection function. In our case, this is the shape of the x-ray induced change to the optical spectral transmission function $\Delta T(\lambda)$. In practice, we take a typical spectral transmission trace, such as that shown in black in the upper panel of Fig. 3, and smooth the waveform slightly to suppress noise. The digital filter operation calculates the correlation function between this typical waveform and the measured signal. The result is a correlation waveform with a linear response to the expected signal, e.g., the peaked function of λ shown in gray in the top panel of Fig. 3. This correlation waveform scales as $h = \beta R^{-1}s$, where s is the noise free signal, R is the noise covariance matrix, and β is a normalization constant such that the convolution peak equals the maximum transmission change in the sampled signal. The noise covariance matrix R is computed from the waveform samples preceding x-ray exposure, e.g., $\Delta T(\lambda > 550\ \text{nm})$ in the case of Fig. 3. This noise covariance matrix is dominated by shot noise from the spectrometer CCD camera, noise in the signal and reference spectra themselves, and errors in the reference spectrum determination. In practice, the reference spectrum errors vary considerably between setups, so optimal filter weights are approximated by the sampled signal waveform offset so that the sum of samples is zero ($\sum_i (s_i - \langle s \rangle)$). The input signal waveform used in the filter weights calculation is extracted from individual events representative of the material used. The bottom plot in Fig. 3 shows an example signal spectrum (black) and the reference spectrum (gray). Also in Fig. 3, the computed relative transmission change is shown on top (black) along with the resulting correlation waveform (gray).

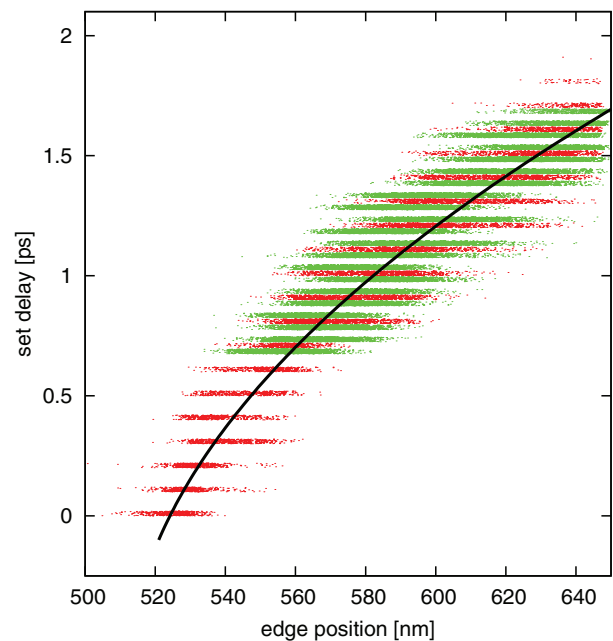


FIG. 4. Delay calibration of chirp. We show the delay calibration for two separate Si_3N_4 cases. The red points correspond to a $2\ \mu\text{m}$ thick Si_3N_4 membrane while the green points correspond to a $500\ \text{nm}$ thick membrane taken later during the same experiment. The scan was made with discrete steps but we have added an artificial random jitter in the delay coordinate to help represent the density of points. The delay steps were made by adjusting the phase angle of the FEL/optical synchronization loop.

The mapping of the location of the peak in the convolution to relative x-ray arrival time is set by the chirp of the continuum pulse. We perform a delay scan periodically throughout an experiment to confirm the calibration of pixel position to relative delay as shown in Fig. 4 where the peaked convolution curve is fit to locate the relative arrival time. The second order polynomial accounts for both the first and second order chirp as well as the $\lambda \propto 1/\omega$ effect of measuring in wavelength rather than directly in frequency. Figure 4 shows this peak location in pixels correlated with the controlled relative time delay in femtoseconds. Typical dispersive materials produce higher order dispersion as well as the desired linear dispersion for the time-to-frequency mapping. Since, the spectrometer records spectrum linearly in $\lambda \propto 1/\omega$, time is encoded via low-order polynomial in pixels. Consequently, the signal shape varies across the spectrum, and the matched filter becomes slightly less effective at finding the signal. This results in an underestimate of the signal amplitude and a slight shift in the determination of the relative arrival time since the shape deviates from the characteristic input from which the weights were derived.

The most obvious improvement would be to remap the spectral components into frequency space. We calibrate the wavelength against an Ocean Optics HG-1 Mercury/Argon low-pressure gas source. Based on the known lines, we map the CCD pixels to frequency (PHz optical regime). By first applying the Jacobian transformation of the measured wavelength spectrum to the frequency representation, we begin to see the significance of the finer features of the signal.

Besides the step in the spectrum, which we fit via the matched filtering routine, the transmitted spectrum through

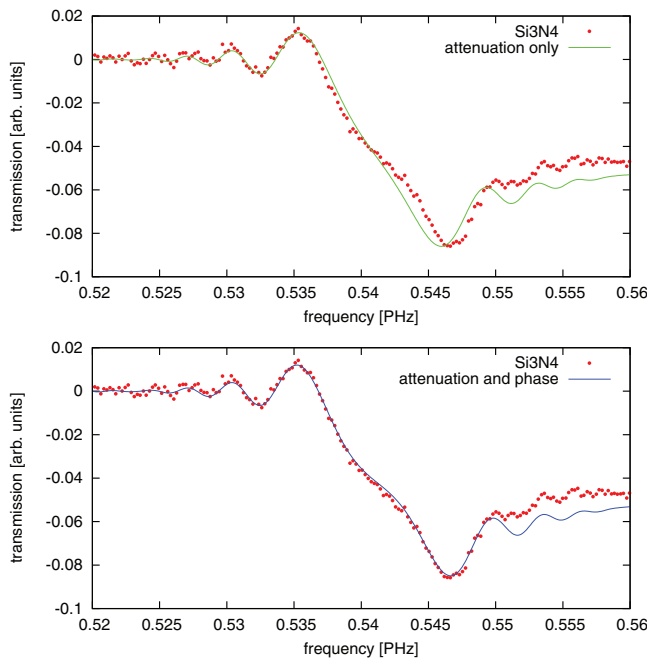


FIG. 5. Typical response waveform. The red dotted line shows a typical response waveform from Si_3N_4 . Lines show a simulated response function using absorption only (green) or absorption and phase (blue).

silicon nitride produces fine structure on either side of the step as well as a shoulder within the step itself. This fine structure carries information about the transiently induced index change. We can readily investigate this in simulation by changing both the real and imaginary components of the refractive index. By simulating not only an amplitude modulation but also a phase modulation, we recover the complex modulation of the material index as seen in Fig. 5.

IV. SCALING

As a simple rule of thumb, assuming the continuum is sampling only the spatial center of the x-ray spot, the signal amplitude, Δ , can be estimated by scaling measured results for Si_3N_4 ($\Delta|_{\text{ref.}}$) for the differences in material absorption, sample thickness, and x-ray pulse fluence,

$$\Delta = \kappa F(1 - e^{-T/\alpha}), \quad (1)$$

Here Δ is the change in transmission measured as (signal-reference)/reference, κ is a scale factor of $0.01 \text{ cm}^2/\text{mJ}$, F is the x-ray fluence in mJ/cm^2 , T is the interaction thickness, and α is the absorption length. The edge finding algorithms work very well for signal strengths of $\Delta \geq 0.05$. Figure 3 shows a typical 10% change in transmission signal ($\Delta = 0.1$). The fluence F can be controlled by the intensity of the x-ray pulses as well as their focus. The signal increases linearly with x-ray fluence until it nears saturation for transmission changes exceeding 50% as indicated in Figs. 9(a) and 9(c). For samples with x-ray penetration depths much longer than the sample thickness, the signal is linear in thickness as well. Therefore, the 10% signal change in transmission can be achieved by balancing sample thickness and x-ray spot size at the sample for a given x-ray wavelength and

pulse energy. For example, based on our estimated spot size, to achieve a signal at this 10% level, $8 \text{ mJ}/\text{cm}^2$ must be absorbed by the Si_3N_4 membrane at 9 keV hard x-rays. At soft x-rays, e.g., 1 keV, a thinner Si_3N_4 sample with smaller x-ray spot and lower power, but conserving the deposited energy density, is within a factor of two of this estimate. Because the signal is determined by absorbed fluence, the sample thickness therefore depends on the material absorption length and x-ray pulse energy and spot size for a given photon energy. Table I presents typical values used at the LCLS. Controlling the x-ray spot size helps to balance the required thickness due to temporal walkoff.

The intrinsic optical properties of Si_3N_4 in the x-ray regime make it an ideal material for a time tool. The ability to work with thin membranes addresses the group delay problem while the ease of producing a variety of thicknesses makes adjusting the balance between thickness, x-ray wavelength, pulses energy, and spot size much more flexible. In the hard x-ray regime, Si_3N_4 has very low absorption cross section yet the induced optical modulation is sufficient for a good signal to noise ratio. Enough signal is made even when placed downstream of the hard x-ray monochromator, which decreases the x-ray flux to about $\sim 3\%$. With the low absorption for Si_3N_4 at hard x-ray wavelengths, cross-correlation measurements can be taken upstream of the experimental interaction region without significantly decreasing the x-ray flux delivered to the experiment. Other materials such as diamond and quartz have been pursued but none appear to have quite the flexibility of silicon nitride for soft x-rays and Ce:YAG for hard x-rays.

V. DISCUSSION

Information about the changing material properties can be extracted from the fine structure wiggles as seen in Fig. 5. One would like to understand the x-ray induced changes for various materials as seen in Fig. 6. For each material, the x-ray pulse modulates the absorption and phase with different ratios, thus the shape of the step is unique to each specific material. We summarize some of the optical and x-ray properties for materials so far studied in Table I. These different shapes indicate the x-ray induced electron dynamics that send a cascade of electrons to increase conduction band occupancy.³³ Depending on material and photon energy, this cascade can take from 30 to 100 fs.^{23,34,35} FEL pulses, typical of Self Amplification of Spontaneous Emission (SASE), exhibit complicated temporal structure. This structure is much finer than these typical cascade time for these materials used, and therefore the material response effectively acts as a smoothing filter over the FEL pulses.³⁵ Because of this, these measurements are sensitive to the temporal centroid of the x-ray pulse.

Diamond exhibits a carrier response that is potentially faster than silicon nitride.³⁴ At these fluences, contrary to silicon nitride, the “step” in diamond is created primarily by modulation of the real part of the index of refraction as shown in Fig. 7. Thus, the material is nearly equally transmissive before and after the x-ray pulse, so the intensity of the transmitted spectrum remains nearly the same. We note that at fluence levels closer to the damage threshold diamond begins to

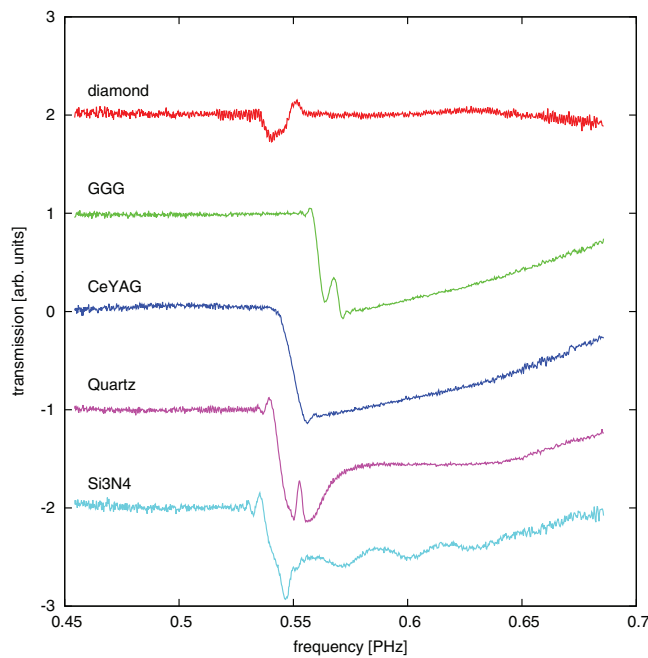


FIG. 6. Material responses. Typical examples of the x-ray induced transmission change for various materials. Reprinted with permission from M. R. Bionta, D. French, J. Cryan, J. M. Glowina, N. Hartmann, D. J. Nicholson, K. Baker, C. Bostedt, M. Cammarrata, M. Chollet, Y. Ding, D. M. Fritz, S. M. Durbin, Y. Feng, M. Harmand, A. R. Fry, D. J. Kane, J. Krzywinski, H. T. Lemke, M. Messerschmidt, D. Ratner, S. Schorb, S. Toleikis, D. Zhu, W. E. White, and R. Coffee, *Proc. SPIE* **8504**, 85040M (2012). Copyright 2012 SPIE and the authors.¹⁹

exhibit a step-like function. Crystalline quartz displays roughly equal phase and absorption contributions. In all cases, this spectral interferometry acts as a homodyne detection, whose spectral width of interference inversely corresponds to the temporal width of the material response. Details of the particular response of various materials are the subject of on going research beyond the scope of this instrument review.

One complication of a thin film transmission experiment is the appearance of etalon effects. The etalon arises from the multiple reflections of the continuum pulse at the front and back surfaces of the film. Since thicker materials are often used to compensate the low absorption cross-section at harder x-rays, etalon contributions are observed as seen in Fig. 8 and the inset in Fig. 7. Shown in Fig. 8, the magnitude of the central shoulder also varies with the etalon modulation. Including

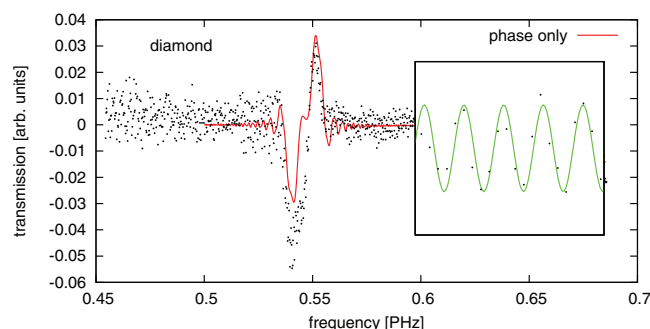


FIG. 7. Diamond. Hard x-ray modulation in diamond. We note that the spread in data points are the etalon effect induced by the $55\ \mu\text{m}$ thick diamond sample (inset).

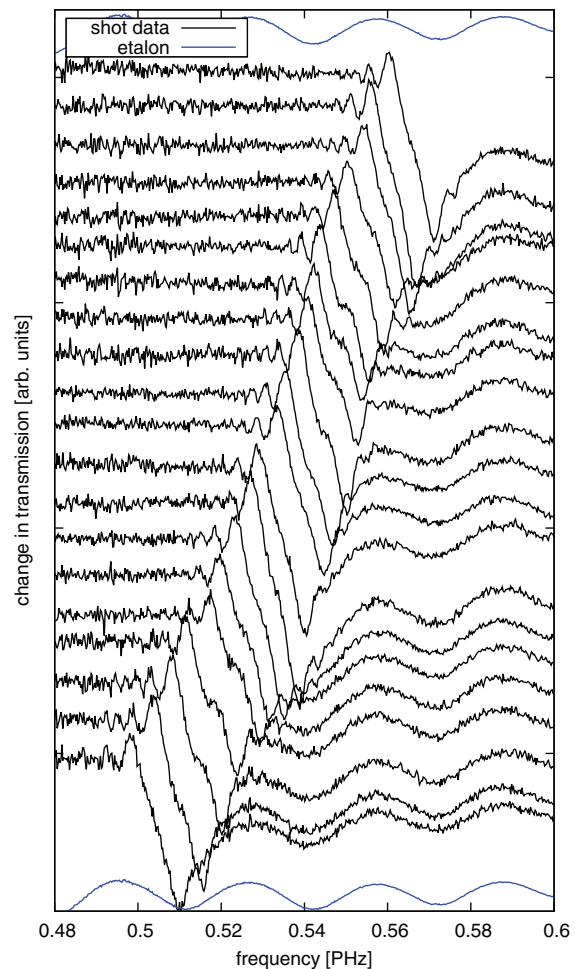


FIG. 8. Etalon effects. The effective etalon thickness changes following the x-ray interaction. This is seen in the appearance of ripples in the difference (signal–reference).

this effect in the edge finding algorithm would eliminate the slight systematic error in locating the edge; possibly explaining the slight “s” curve in the correlation of supplementary Fig. 5 (lower left panel) of Ref. 23. We note that the etalon effect in Fig. 9 is the most likely culprit for systematic frequency to time mapping errors. In addition, one could also independently monitor the spectral phase in a separate dispersion matched arm.

One might consider transmitting the x-rays and continuum through the membrane at Brewster’s angle, thus removing the surface reflections that produce the etalon. We can however include the etalon effect in the fitting algorithm itself, removing systematic errors by properly modeling the interaction. In fact, it may be beneficial to retain the etalon effect if for no other reason than finding coarse time overlap since this change typically lasts for many picoseconds as discussed in Sec. II A.

As an alternative to computationally expensive modeling, we could pursue a pattern discovery technique that optimally accounts for the various parameters used to identify relative arrival time. The most highly correlated parameters are the following five values for every shot: edge fit position, width, amplitude, x-ray energy, and set delay. We will use the

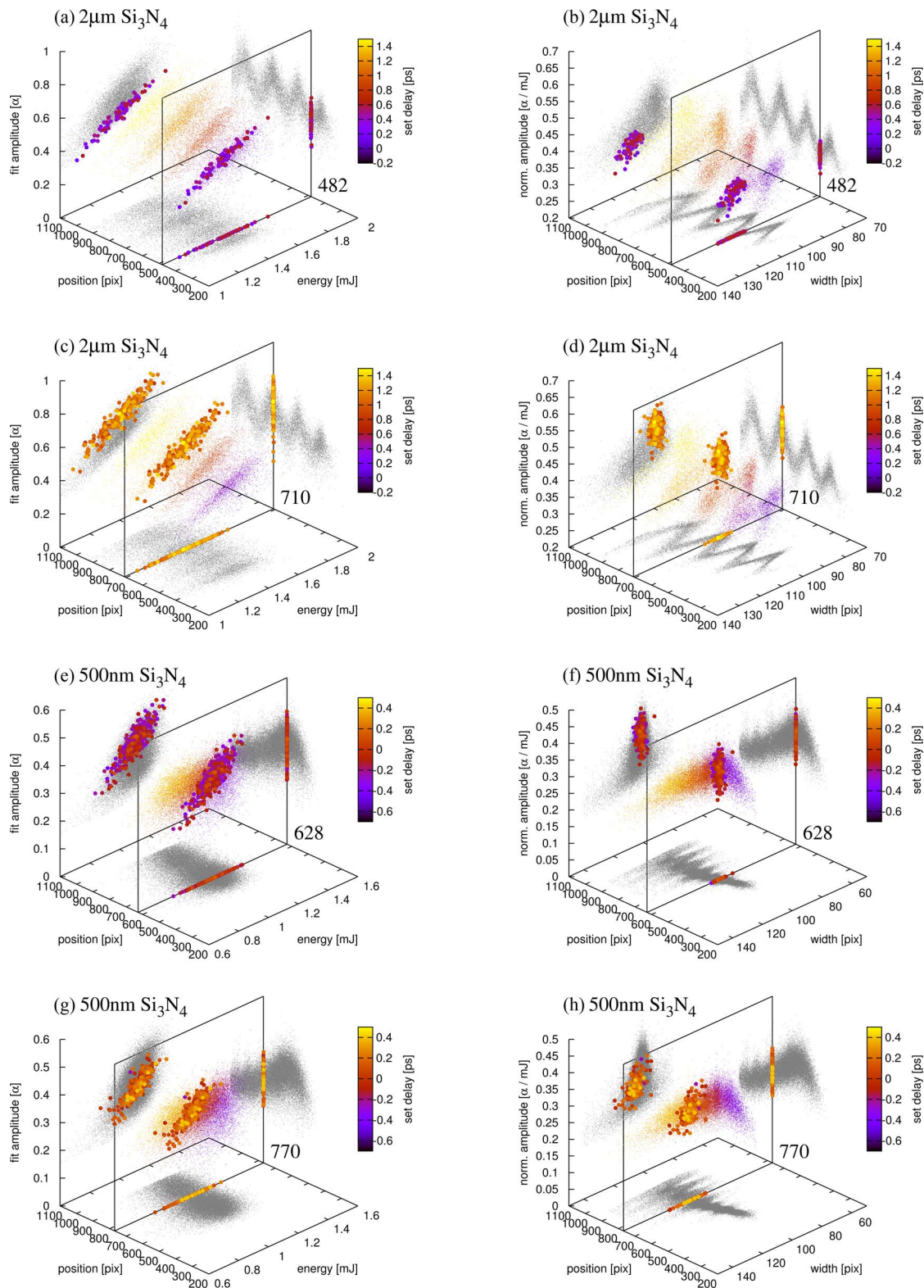


FIG. 9. Matched filter results. Here, we show different slices of various output parameters from the matched filter routine as applied directly to the wavelength-representation spectrum. We note that each data point represents the fit results from a single shot of the FEL. (Multimedia view) [[URL: http://dx.doi.org/10.1063/1.4893657.1](http://dx.doi.org/10.1063/1.4893657.1)]

multimedia view of Fig. 9 (Multimedia view) to facilitate the pattern recognition. We treat these five values for each shot as coordinates in a five-dimensional phase space such that every displayed point represents a single shot. In Fig. 9 (Multime-

dia view), we represent three of the dimensions in orthogonal Cartesian space and use color, in all panels, to represent the externally set x-ray/optical relative delay value in picoseconds for that particular shot. Also in all panels, the bottom left axis

represents the matched-filter edge position in pixels. Panels (a)–(d) show the correlation relationships sliced at different peaks in the corrugation. Panels (e)–(h) show the same but for a 500 nm thick Si_3N_4 membrane. To aid the eye, we also show wall projections of the active sliced data points (color) along with the full projected set (gray). In the left panels ((a), (c), (e), and (g)), the vertical axis represents matched-filter amplitude in arbitrary units [α] while the lower right axis represents x-ray pulse energy in mJ. For a given slice in position, lower left axis, we find a linear correlation between amplitude α and x-ray pulse energy as expected. This linear correlation however varies with the etalon induced corrugation. In the right panels ((b), (d), (f), and (h)), we use the vertical axis to represent the proportionality α/mJ and find that it indeed varies by 20%–30% in value with the etalon. Furthermore, this allows us to use the lower right axis to represent the width of the fit edge in pixels. We find that this width also is systematically yet predictably affected by the etalon. We can clearly identify the corrugated relationship between the proportionality α/mJ , the fit width, and the fit position relative to the etalon. For the 500 nm thick Si_3N_4 shown in panels (e)–(h), we see that this effect of the etalon shows an expected factor of 4 longer corrugation period. One could use this pattern not for designing a system that avoids etalon, but rather for using that corrugated relationship directly in a predictive analysis.

VI. CONCLUSION

The cross-correlation technique of spectral encoding, the relative arrival time between an x-ray pulse and an optical laser pulse as described here, is now being standardized across most hutchches at the LCLS. Measurement errors from this technique are typically below 10 fs rms and therefore it has gained interest from other facilities such as the European XFEL and the SwissFEL. Developing this technique further requires a detailed investigation of free-carrier evolution in the materials typical of the measurement. Ongoing analysis of 2-dimensional spectrogram data should reveal the carrier evolution for at least some of these materials. Once that evolution is known, more accurate material response functions can be used in the edge finding algorithm in order to deliver even more precise relative timing information with minimal systematic impact. The ease of implementation and general applicability for hard x-ray, soft x-ray, and even ultraviolet wavelengths make spectral encoding a promising method of relative arrival time tagging.

ACKNOWLEDGMENTS

We would like to acknowledge important discussions regarding applicability and future considerations with Dr. Serguei Molodtsov and Dr. Jan Greunert of the European xFEL consortium as well as Dr. Rafael Abela, Dr. Bruce Patterson, Dr. Christoph Hauri, and Dr. Luc Patthey from the SwissFEL project. For his important technical insight regarding the use of spectral interferometry we thank Dr. Sebastien Weber currently at CEA Saclay. We would like to also acknowledge our close collaboration with Dr. Marion Harmand of CNRS-

Ecole Polytechnique and Dr. Marco Cammarata of University of Rennes.

This research was carried out at the Linac Coherent Light Source (LCLS) at the SLAC National Accelerator Laboratory. LCLS is an Office of Science User Facility funded under the auspices of the U.S. Department of Energy Office of Science operated by Stanford University.

- ¹P. Emma, R. Akre, J. Arthur, R. Bionta, C. Bostedt, J. D. Bozek, A. Brachmann, P. H. Bucksbaum, R. Coffee, F.-J. Decker, Y. Ding, D. Dowell, S. Edstrom, A. Fisher, J. Frisch, S. Gilevich, J. Hastings, G. Hays, P. Herling, Z. Huang, R. Iverson, H. Loos, M. Messerschmidt, A. Miahnahri, S. Moeller, H.-D. Nuhn, G. Pile, D. Ratner, J. Rzepiela, D. Schultz, T. Smith, P. Stefan, H. Tompkins, J. Turner, J. Welch, W. White, J. Wu, G. Yocky, and J. Galayda, *Nat. Photonics* **4**, 641 (2010).
- ²B. Steffen, V. Arsov, G. Berden, W. A. Gillespie, S. P. Jamison, A. M. MacLeod, A. F. G. van der Meer, P. J. Phillips, H. Schlarb, B. Schmidt, and P. Schmüser, *Phys. Rev. Spec. Top. – Accel. Beams* **12**, 032802 (2009).
- ³J. Feldhaus, *J. Phys. B: At., Mol. Opt. Phys.* **43**, 194002 (2010).
- ⁴A. Azima, S. Düsterer, P. Radcliffe, H. Redlin, N. Stojanovic, W. Li, H. Schlarb, J. Feldhaus, D. Cubaynes, M. Meyer, J. Dardis, P. Hayden, P. Hough, V. Richardson, E. T. Kennedy, and J. T. Costello, *Appl. Phys. Lett.* **94**, 144102 (2009).
- ⁵T. Ishikawa, H. Aoyagi, T. Asaka, Y. Asano, N. Azumi, T. Bizen, H. Ego, K. Fukami, T. Fukui, Y. Furukawa, S. Goto, H. Hanaki, T. Hara, T. Hasegawa, T. Hatsui, A. Higashiya, T. Hirono, N. Hosoda, M. Ishii, T. Inagaki, Y. Inubushi, T. Itoga, Y. Joti, M. Kago, T. Kameshima, H. Kimura, Y. Kirihara, A. Kiyomichi, T. Kobayashi, C. Kondo, T. Kudo, H. Maesaka, X. M. Maréchal, T. Masuda, S. Matsubara, T. Matsumoto, T. Matsushita, S. Matsui, M. Nagasono, N. Nariyama, H. Ohashi, T. Ohata, T. Ohshima, S. Ono, Y. Otake, C. Saji, T. Sakurai, T. Sato, K. Sawada, T. Seike, K. Shirasawa, T. Sugimoto, S. Suzuki, S. Takahashi, H. Takebe, K. Takeshita, K. Tamasaku, H. Tanaka, R. Tanaka, T. Tanaka, T. Togashi, K. Togawa, A. Tokuhisa, H. Tomizawa, K. Tono, S. Wu, M. Yabashi, M. Yamaga, A. Yamashita, K. Yanagida, C. Zhang, T. Shintake, H. Kitamura, and N. Kumagai, *Nat. Photonics* **6**, 540 (2012).
- ⁶G. Geloni, E. Saldin, L. Samoylova, E. Schneidmiller, H. Sinn, T. Tschentscher, and M. Yurkov, *New J. Phys.* **12**, 035021 (2010).
- ⁷B. D. Patterson, R. Abela, H.-H. Braun, U. Flechsig, R. Ganter, Y. Kim, E. Kirk, A. Oppelt, M. Pedrozzi, S. Reiche, L. Rivkin, T. Schmidt, B. Schmitt, V. N. Strocov, S. Tsujino, and A. F. Wrulich, *New J. Phys.* **12**, 035012 (2010).
- ⁸E. Allaria, C. Callegari, D. Cocco, W. M. Fawley, M. Kiskinova, C. Masciovecchio, and F. Parmigiani, *New J. Phys.* **12**, 075002 (2010).
- ⁹E. Allaria, D. Castronovo, P. Cinquegrana, P. Craievich, M. Dal Forno, M. B. Danailov, G. D'Auria, A. Demidovich, G. De Nino, S. Di Mitri, B. Diviacco, W. M. Fawley, M. Ferianis, E. Ferrari, L. Froehlich, G. Gaio, D. Gauthier, L. Giannessi, R. Ivanov, B. Mahieu, N. Mahne, I. Nikolov, F. Parmigiani, G. Penco, L. Raimondi, C. Scafuri, C. Serpico, P. Sigalotti, S. Spampinati, C. Spezzani, M. Svandrlik, C. Svetina, M. Trovo, M. Veronese, D. Zangrando, and M. Zangrando, *Nat. Photonics* **7**, 913 (2013).
- ¹⁰I. Hwang, J.-H. Han, Y. Parc, and J. Lee, *J. Korean Phys. Soc.* **64**, 212 (2014).
- ¹¹P. Oberta, U. Flechsig, and R. Abela, *Proc. SPIE* **8078**, 807805 (2011).
- ¹²F. Löhler, V. Arsov, M. Felber, K. Hacker, W. Jalmuzna, B. Lorbeer, F. Ludwig, K.-H. Matthiesen, H. Schlarb, B. Schmidt, P. Schmüser, S. Schulz, J. Szewinski, A. Winter, and J. Zemella, *Phys. Rev. Lett.* **104**, 144801 (2010).
- ¹³J. M. Glowina, J. Cryan, J. Andreasson, A. Belkacem, N. Berrah, C. I. Blaga, C. Bostedt, J. D. Bozek, L. F. DiMauro, L. Fang, J. Frisch, O. Gessner, M. Gühr, J. Hajdu, M. P. Hertlein, M. Hoener, G. Huang, O. Kornilov, J. P. Marangos, A. M. March, B. K. McFarland, H. Merdji, V. S. Petrovic, C. Raman, D. Ray, D. A. Reis, M. Trigo, J. L. White, W. White, R. Wilcox, L. Young, R. Coffee, and P. H. Bucksbaum, *Opt. Express* **18**, 17620 (2010).
- ¹⁴S. Schorb, T. Gorkhover, J. Cryan, J. M. Glowina, M. R. Bionta, R. Coffee, B. Erk, R. Boll, C. Schmidt, D. Rolles, A. Rudenko, A. Rouzee, M. Swiggers, S. Carron, J.-C. Castagna, J. D. Bozek, M. Messerschmidt, W. F. Schlotter, and C. Bostedt, *Appl. Phys. Lett.* **100**, 121107 (2012).
- ¹⁵M. Beye, O. Krupin, G. Hays, A. H. Reid, D. Rupp, S. de Jong, S. Lee, W. S. Lee, Y. D. Chuang, R. Coffee, J. Cryan, J. M. Glowina, A. Föhlisch, M. R. Holmes, A. R. Fry, W. E. White, C. Bostedt, A. O. Scherz, H. A. Durr, and W. F. Schlotter, *Appl. Phys. Lett.* **100**, 121108 (2012).

- ¹⁶T. Maltezopoulos, S. Cunovic, M. Wieland, M. Beye, A. Azima, H. Redlin, M. Krikunova, R. Kalms, U. Frühling, F. Budzyn, W. Wurth, A. Föhlisch, and M. Drescher, *New J. Phys.* **10**, 033026 (2008).
- ¹⁷C. Gahl, A. Azima, M. Beye, M. Deppe, K. Döbrich, U. Hasslinger, F. Hennies, A. Melnikov, M. Nagasono, A. Pietzsch, M. Wolf, W. Wurth, and A. Föhlisch, *Nat. Photonics* **2**, 165 (2008).
- ¹⁸M. R. Bionta, J. Cryan, J. M. Glownia, D. French, C. Bostedt, M. Cammarrata, J.-C. Castagna, Y. Ding, S. M. Durbin, Y. Feng, A. Fry, D. J. Kane, J. Krzywinski, H. Lemke, M. Messerschmidt, A. Natan, D. Ratner, S. Schorb, M. Swiggers, M. Trigo, W. White, and R. Coffee, *CLEO: QELS-Fundamental Science*, OSA Technical Digest (Optical Society of America, 2012), p. QTu2H.5.
- ¹⁹M. R. Bionta, D. French, J. Cryan, J. M. Glownia, N. Hartmann, D. J. Nicholson, K. Baker, C. Bostedt, M. Cammarrata, M. Chollet, Y. Ding, D. M. Fritz, S. M. Durbin, Y. Feng, M. Harmand, A. R. Fry, D. J. Kane, J. Krzywinski, H. T. Lemke, M. Messerschmidt, D. Ratner, S. Schorb, S. Toleikis, D. Zhu, W. E. White, and R. Coffee, *Proc. SPIE* **8504**, 85040M (2012).
- ²⁰A. Couairon and A. Mysyrowicz, *Phys. Rep.* **441**, 47 (2007).
- ²¹Y.-H. Chen, S. Varma, I. Alexeev, and H. Milchberg, *Opt. Express* **15**, 7458 (2007).
- ²²I. Wilke, A. MacLeod, W. Gillespie, G. Berden, G. Knippels, and A. van der Meer, *Phys. Rev. Lett.* **88**, 124801 (2002).
- ²³M. Harmand, R. Coffee, M. R. Bionta, M. Chollet, D. French, D. Zhu, D. M. Fritz, H. T. Lemke, N. Medvedev, B. Ziaja, S. Toleikis, and M. Cammarrata, *Nat. Photonics* **7**, 215 (2013).
- ²⁴M. R. Bionta, H. T. Lemke, J. Cryan, J. M. Glownia, C. Bostedt, M. Cammarrata, J.-C. Castagna, Y. Ding, D. M. Fritz, A. R. Fry, J. Krzywinski, M. Messerschmidt, S. Schorb, M. L. Swiggers, and R. Coffee, *Opt. Express* **19**, 21855 (2011).
- ²⁵C. D. Amico, A. Houard, S. Akturk, Y. Liu, J. Le Bloas, M. Franco, B. Prade, A. Couairon, V. T. Tikhonchuk, and A. Mysyrowicz, *New J. Phys.* **10**, 013015 (2008).
- ²⁶S. Tzortzakis, G. Méchain, G. Patalano, M. Franco, B. Prade, and A. Mysyrowicz, *Appl. Phys. B* **76**, 609 (2003).
- ²⁷G. Turin, *Proc. IEEE* **64**, 1092 (1976).
- ²⁸B. Henke, E. Gullikson, and J. Davis, *At. Data Nucl. Data Tables* **54**, 181 (1993).
- ²⁹M. Bass, C. DeCusatis, J. Enoch, V. Lakshminarayanan, G. Li, C. MacDonald, V. Mahajan, and E. Van Stryland, *Handbook of Optics, Volume I: Geometrical and Physical Optics, Polarized Light, Components and Instruments(set)*, 3rd ed. (McGraw-Hill, Inc., New York, NY, USA, 2010).
- ³⁰S. Webb, "X-ray utilities," Mobile Application, Version 1.1, 2010.
- ³¹D. L. Wood and K. Nassau, *Appl. Opt.* **29**, 3704 (1990).
- ³²D. E. Aspnes and A. A. Studna, *Phys. Rev. B* **27**, 985 (1983).
- ³³R. Riedel, A. Al-Shemmary, M. Gensch, T. Golz, M. Harmand, N. Medvedev, M. J. Prandolini, K. Sokolowski-Tinten, S. Toleikis, U. Wegner, B. Ziaja, N. Stojanovic, and F. Tavella, *Nat. Commun.* **4**, 1731 (2013).
- ³⁴B. Ziaja, R. A. London, and J. Hajdu, *J. Appl. Phys.* **97**, 064905 (2005).
- ³⁵N. Hartmann, W. Helml, A. Galler, M. R. Bionta, J. Grünert, S. L. Molodtsov, K. R. Ferguson, S. Schorb, M. L. Swiggers, S. Carron, C. Bostedt, J.-C. Castagna, J. Bozek, J. M. Glownia, D. J. Kane, A. R. Fry, W. E. White, C. P. Hauri, T. Feurer, and R. N. Coffee, "Sub-femtosecond precision measurement of relative X-ray arrival time for free-electron lasers," *Nat. Photonics* (published online 2014).